PPr801 Project Report
on

Helioseismic Inversion for Rotation Rate

submitted by

Vishal Sai Vetrivel

Roll No: P0211557

Under the guidance of

Prof. H.M Antia

Department of Physical Sciences

Centre for Excellence in Basic Sciences

Mumbai - 400098

April 2025

Certificate

This is to clarify that CEBS student Vishal Sai Vetrivel has undertaken project work from 1st January 2025 to 1st May 2025 under the guidance of Prof. H M Antia
This submitted project report titled Helioseismic Inversion for Rotation Rate is towards the academic requirements of the M.Sc. program's 8th Semester Project Course at UM-DAE CEBS.

Vishal Sai Vetrivel
01-05-2025
Name and Signature of Student with Date

H. M. Antia
01-05-2025
Name and Signature of Advisor(s) with Date

Acknowledgments

I would like to express my gratitude to my guide Prof. H M Antia for his invaluable feedback in the writing of this report.

I would also like to thank Dr. Jørgen Christensen-Dalsgaard for publicly uploading his Lecture notes on Stellar Oscillations.

This project uses data acquired by GONG instruments operated by NISP/NSO/AURA/NSF with contribution from NOAA and from the HMI on board the SDO operated by NASA.

Abstract

Helioseismology, the study of the solar interior using oscillations observed at the Solar Surface have been instrumental in our understanding of solar structure and dynamics. The high accuracy with which these observations can be made in the case of the Sun allow us to make confident inferences on our Solar and Stellar models. In this project we study the inverse problem for rotation in the solar interior and use Regularized Least Squares (RLS) method to perform inversion.

Contents

1. Introduction

Helioseismology is the study of the structure and dynamical properties of the Sun by its oscillations. These oscillations were first discovered by Leighton et al. [1962] who measured the Doppler shift in a solar spectral line and found periodic oscillations with a period of about 5 minutes. These were explained to be the normal modes of the Sun by (Ulrich [1970]; Leibacher and Stein [1971]) and later confirmed by (Deubner [1975]). Early observations did not have the spatial or temporal resolution to resolve individual modes however, with newer instruments this is now possible with precise measurements of nearly 10^6 modes. This was made possible due to long duration nearly continuous observation of the Sun which allowed us to resolve the frequencies with much higher precision. There are two types of observations of solar oscillations. First is to observe integrated light over the whole disk of the Sun. This method is only capable of resolving low order modes with large length scales. While this is not useful for our purposes it gives a good proxy for Asteroseismology as when observing distant stars the integrated light is usually all that is possible. The second method is to resolve the Doppler shift velocities of the Sun resolved over a grid. There are three major instruments that provide the best data for this method, they are GONG (Global Oscillations Network Group), HMI (Helioseismic and Magnetic Imager) and MDI (Michelson Doppler Imager). We will be using data from the first two instruments in this project.

The theory of solar oscillations initially assumes a equilibrium state at rest. If we consider small adiabatic perturbations to this equilibrium state we obtain the equations for linear adiabatic oscillations. The eigenvalues of these equations give the frequencies of solar oscillations. For spherically symmetric Sun the frequencies are independent of azimuthal order m, which defines the spherical harmonics. The presence of rotation however breaks this degeneracy giving rotational splitting of modes, which can be used to infer the rotation rate of the solar interior.

In this work we study the rotation rate of solar interior using inversion techniques. We setup the inverse problem using variational techniques. We have used the Regularized Least Squares method to solve the inverse problem. We have also analyzed the temporal variation of rotation rate over 30 years and two complete solar cycles.

2. Data used in the Study

These data used in this project are from two different sources. The first is 5 year data starting from 2010 on the frequencies and splitting coefficients which are obtained from the Helioseismic and Magnetic Imager (HMI) Scherrer et al. [2012] which is on board the Solar Dynamics Observatory (SDO) launched by NASA in 2010. The HMI is a space based instrument which images the entire solar disk nearly continuously at 6173 Å with a resolution of 1 arcsecond. This data contains the frequencies and splitting coefficients for modes with $l \leq 300$. The long time series allows us to determine the rotation rate accurately in most of the solar interior.

We also use data from the Global Oscillations Network Group (GONG) to calculate the temporal variance of rotation rate. GONG is a network of 6 ground based telescopes that have been actively collecting data from 1995. It has an effective resolution of 5 arcseconds and was upgraded to a 1000x1000 CCD in 2001. The 6 different sites allow the network to keep up almost 90% coverage of the Sun 24/7 (Harvey et al. [1996]). We will be using the splitting data which are computed for a combined 3-GONG month time series (108 days as 1 GONG month = 36 days), centered on the second month with an overlap of 2 months on both sides. We will use data spanning 300 GONG months from 1995 to 2025. These data contain the same parameters as HMI but only for modes up to $l = 150$. This is due to the fact that GONG is a ground based telescope which is affected by atmospheric interference leading to low spatial resolution. This data can be downloaded from the GONG NSO archive at

https://gong2.nso.edu/archive/patch.pl

3. The Inverse Problem

Chandrasekhar [1964] showed that the operator used in the equation of adiabatic oscillations is Hermitian. This means that variational principle may be used to perform perturbation analysis on the problem. This allows us to study the effect of perturbation to the equations from departures from the simple approximate case such as rotation.

To get the corresponding operator we perturb the steady equilibrium solar model by considering small perturbations to the basic variables:-

$$\rho = \rho_0 + \rho_1, \qquad p = p_0 + p_1, \qquad \phi = \phi_0 + \phi_1, \tag{3.1}$$

$$\omega^2 \rho_0 \boldsymbol{\xi} = \boldsymbol{\nabla} p_1 - \boldsymbol{g}\rho_1 + \rho_0 \boldsymbol{\nabla}\phi_1, \tag{3.2}$$

where ρ is the density, p is the pressure, $\boldsymbol{g}$ is the gravitational acceleration, ϕ is the gravitational potential, ξ is the displacement due to perturbation and we will later assume the perturbation is oscillatory which will have ω as the frequency. The quantities with subscript 0 are the equilibrium values and are taken to be static and spherically symmetric whereas the perturbations are written with subscript 1 and are assumed to be small. We can use the continuity equation and adiabatic condition to eliminate p_1, ρ_1 and ϕ_1

$$\rho_1 = -\boldsymbol{\nabla} \cdot (\rho_0 \boldsymbol{\xi}), \tag{3.3}$$

$$p_1 = c_0^2 \rho_1 - \rho_0 c_0^2 \boldsymbol{\xi_r} \frac{\mathcal{N}^2}{g_0}, \tag{3.4}$$

$$c_0^2 = \frac{\Gamma_{1,0} p_0}{\rho_0}, \tag{3.5}$$

$$\phi_1(\boldsymbol{r}) = -G \int_{V'} \frac{\rho_1(\boldsymbol{r'})\, dV'}{|\boldsymbol{r} - \boldsymbol{r'}|}, \tag{3.6}$$

here c_0 is sound speed. ρ_1 in (3.6) can be eliminated using (3.3). Here $\mathcal{N}^2$ is Brunt–Väisälä frequency and is given by

$$\mathcal{N}^2 = g_0 \left(\frac{1}{\Gamma_{1,0}} \frac{d \ln p_0}{dr} - \frac{d \ln \rho_0}{dr} \right), \tag{3.7}$$

where $\Gamma_{1,0}$ is an adiabatic exponent. These two equations can be used with (3.2) to yield an equation in terms of $\boldsymbol{\xi}$ as follows:-

$$\mathcal{L}\boldsymbol{\xi} = \rho_0 \omega^2 \boldsymbol{\xi}, \tag{3.8}$$

where $\mathcal{L}$ is a Hermitian operator. The eigenfunctions of this equation $\boldsymbol{\xi}$ are taken in the following form which allows separation of variables and leads to equations in only radial coordinates:-

$$\boldsymbol{\xi(r,t)} = \left(\xi_r(r)\, Y_l^m \hat{\boldsymbol{r}} + \xi_h(r) \left(\frac{\partial Y_l^m}{\partial \theta} \hat{\boldsymbol{\theta}} + \frac{1}{\sin\theta} \frac{\partial Y_l^m}{\partial \phi} \hat{\boldsymbol{\phi}} \right) \right) e^{-i\omega t}, \tag{3.9}$$

where ξ_r and ξ_h are the radial and horizontal eigenfunctions respectively and Y_l^m are spherical harmonics. They also satisfy the orthogonality relation:-

$$\left\langle \boldsymbol{\xi}^i, \boldsymbol{\xi}^j \right\rangle = \int_0^{\mathrm{R}_\odot} \left(\boldsymbol{\xi}_r^i \boldsymbol{\xi}_r^j + l(l+1)\, \boldsymbol{\xi}_h^i \boldsymbol{\xi}_h^j \right) \rho_0 r^2 dr = \delta_{ij}, \tag{3.10}$$

This is also an inner product. We don't need a complex conjugate as ξ_h and ξ_r are both real. If we consider a small perturbation to the operator $\mathcal{L}$ and eigenfunction $\boldsymbol{\xi}$ and neglecting higher order terms, we get the following:-

$$(\mathcal{L} + \delta\mathcal{L})(\boldsymbol{\xi} + \delta\boldsymbol{\xi}) = \rho_0 \left(\omega^2 + \delta\omega^2\right)(\boldsymbol{\xi} + \delta\boldsymbol{\xi})$$
$$\mathcal{L}\delta\boldsymbol{\xi} + \delta\mathcal{L}\boldsymbol{\xi} = \rho_0 \delta\omega^2 \boldsymbol{\xi} + \rho_0 \omega^2 \delta\boldsymbol{\xi}.$$

Taking inner product with $\boldsymbol{\xi}$ we get:-

$$\cancel{\langle \boldsymbol{\xi}, \mathcal{L}\delta\boldsymbol{\xi}\rangle} + \langle \boldsymbol{\xi}, \delta\mathcal{L}\boldsymbol{\xi}\rangle = \delta\omega^2 \langle \boldsymbol{\xi}, \boldsymbol{\xi}\rangle + \cancel{\omega^2 \langle \boldsymbol{\xi}, \delta\boldsymbol{\xi}\rangle}.$$

Using the hermiticity of $\mathcal{L}$ we can eliminate a few terms giving:-

$$\delta\omega^2 = 2\omega\delta\omega = \frac{\langle \boldsymbol{\xi}, \delta\mathcal{L}\boldsymbol{\xi}\rangle}{\langle \boldsymbol{\xi}, \boldsymbol{\xi}\rangle}. \tag{3.11}$$

In the case of rotation we assume that we are dealing with a slowly rotating star. If we calculate the ratio of centrifugal force to gravitational force we see that it is about 10^{-5}. This allows us to neglect higher order terms in $\boldsymbol{v_0}(\boldsymbol{r}, \boldsymbol{\theta})$ which is the velocity field of the star at equilibrium. We first write the time derivative of the displacement $\boldsymbol{\xi}$:-

$$\frac{d\boldsymbol{\xi}}{dt} = \frac{\partial \boldsymbol{\xi}}{\partial t} + \boldsymbol{v_0} \cdot \boldsymbol{\nabla}\boldsymbol{\xi}. \tag{3.12}$$

In the inertial frame the velocity $v_0 = \Omega r \sin\theta \hat{\boldsymbol{\phi}}$, where $\Omega(r, \theta)$ is the rotation rate. Calculating the second order derivative we get:-

$$\frac{d^2\boldsymbol{\xi}}{dt^2} = \frac{\partial^2 \boldsymbol{\xi}}{\partial t^2} + 2\boldsymbol{v_0} \cdot \boldsymbol{\nabla}\left(\frac{\partial \boldsymbol{\xi}}{\partial t}\right) + \boldsymbol{v_0} \cdot \boldsymbol{\nabla}\left(\boldsymbol{v_0} \cdot \boldsymbol{\nabla}\boldsymbol{\xi}\right). \tag{3.13}$$

In principle the continuity equation (3.3) will also be changed by the addition of a velocity field but with some considerable manipulation it can be showed that the extra terms cancel. The last term in the above equation is a centrifugal term of order v_0^2 so we may neglect it. This means the perturbation to our operator is given by the second term. Assuming perturbations with time dependence of the form $\exp(-i\omega t)$ we get

$$\delta\mathcal{L}\boldsymbol{\xi} = -2i\omega\rho_0 \boldsymbol{v_0} \cdot \boldsymbol{\nabla}\boldsymbol{\xi} = -2i\omega\rho_0\Omega\frac{\partial \boldsymbol{\xi}}{\partial \phi}. \tag{3.14}$$

Putting this in (3.11) we get

$$\delta\omega = -i\frac{\left\langle \boldsymbol{\xi}, \rho_0\Omega\frac{\partial \boldsymbol{\xi}}{\partial \phi}\right\rangle}{\langle \boldsymbol{\xi}, \boldsymbol{\xi}\rangle}, \tag{3.15}$$

this can be evaluated by computing the derivative $\partial\boldsymbol{\xi}/\partial\phi$. This isn't trivial as the unit vectors $\hat{\boldsymbol{r}}, \hat{\boldsymbol{\phi}}$ and $\hat{\boldsymbol{\theta}}$ aren't constants.

$$\frac{\partial \boldsymbol{\xi}}{\partial \phi} = \frac{\partial}{\partial \phi}\left(\xi_r Y_l^m \hat{\boldsymbol{r}} + \xi_h\left(\frac{\partial Y_l^m}{\partial \theta}\hat{\boldsymbol{\theta}} + \frac{1}{\sin\theta}\frac{\partial Y_l^m}{\partial \phi}\hat{\boldsymbol{\phi}}\right)\right) \tag{3.16}$$

$$= im\boldsymbol{\xi} + \xi_r Y_l^m \sin\theta\hat{\boldsymbol{\phi}} + \xi_h\frac{\partial Y_l^m}{\partial \theta}\cos\theta\hat{\boldsymbol{\phi}} - \frac{\xi_h}{\sin\theta}\frac{\partial Y_l^m}{\partial \phi}\left(\sin\theta\hat{\boldsymbol{r}} + \cos\theta\hat{\boldsymbol{\theta}}\right), \tag{3.17}$$

substituting this in (3.15) and evaluating the ϕ integral we get:-

$$\begin{aligned}\delta\omega \;=\; m\int_0^{\pi}\int_0^{\mathrm{R}_\odot}\Omega\Big[&\xi_r^2 Y_l^m Y_l^{m*} + \xi_h^2\left(\frac{\partial Y_l^m}{\partial\theta}\frac{\partial Y_l^{m*}}{\partial\theta} + \frac{m^2}{\sin^2\theta}Y_l^m Y_l^{m*}\right)\\ &-2\xi_r\xi_h Y_l^m Y_l^{m*} - 2\xi_h^2\cot\theta\frac{\partial Y_l^m}{\partial\theta}Y_l^{m*}\Big]\rho_0 r^2 dr\sin(\theta)\,d\theta/N,\end{aligned} \tag{3.18}$$

where

$$N = \int_0^{\mathrm{R}_\odot}\rho_0\left(\xi_r^2 + L^2\xi_h^2\right)r^2 dr \quad , \quad \left[L^2 = l(l+1)\right]. \tag{3.19}$$

We note that all the theta dependence is in trigonometric functions of sin and cos. This is used to rearrange the equation into the following form

$$\delta\omega = \int_{-1}^{1}\int_0^{\mathrm{R}_\odot} K(r, \cos\theta)\,\Omega(r, \cos\theta)\,dr\,d(\cos\theta), \tag{3.20}$$

where $K(r, \cos\theta)$ is called the kernel.

Since the splitting in frequencies is small it is often represented in the form:-

$$\nu_{nl}^{m} = \nu_{nl} + \sum_{s=1,3,5,\ldots} \gamma_{sl}^{m}\, {}_{n}c_{sl}, \tag{3.21}$$

where the splitting is represented as a expansion in orthogonal polynomials γ_{sl}^{m} of degree s in m that are orthogonal over a discrete sum and ${}_{n}c_{sl}$ are called splitting coefficients.

Ritzwoller and Lavely [1991] have shown that we can write rotational velocity as follows:-

$$v_{rot} = \Omega r \sin\theta = -\sum_{s=1,3,5,\ldots} w_{s}^{0}(r)\, \frac{\partial Y_{s}^{0}}{\partial \theta}, \tag{3.22}$$

where $w_{s}^{0}(r)$ are expansion coefficients. The odd order coefficients in this expansion are North South symmetric and the even order coefficients are N-S anti-symmetric. The kernel itself is N-S symmetric which means only the odd terms will survive the integral and the even terms can be dropped in this step. The even terms will be of use when calculating the N-S anti-symmetric component of rotation which cannot be calculated from global modes. By substituting (3.22) in (3.20) and considerable manipulation using integrals of products of 3 spherical harmonics Ritzwoller and Lavely [1991] have shown that:-

$${}_{n}c_{sl} = \int_{0}^{\mathrm{R}_{\odot}} w_{s}^{0}(r)\, {}_{n}K_{ls}(r)\, r^{2} dr, \tag{3.23}$$

where ${}_{n}K_{ls}(r)$ is given by:-

$${}_{n}K_{ls}(r) = -\rho_{0} r^{-1} \left[\xi_{r}^{2} + L^{2}\xi_{h}^{2} - \left(2\xi_{r}\xi_{h} + \frac{1}{2}s(s+1)\,\xi_{h}^{2}\right)\right]/N. \tag{3.24}$$

By applying orthogonality of spherical harmonics to both sides of (3.22) we get:-

$$w_{s}^{0}(r) = \frac{\sqrt{\pi(2s+1)}}{s(s+1)} \int_{-1}^{1} \Omega(r, \cos\theta) \sin\theta P_{s}^{1}(\cos\theta)\, d(\cos\theta). \tag{3.25}$$

Substituting (3.25) into (3.23) we get

$${}_{n}c_{sl} = \int_{0}^{\mathrm{R}_{\odot}} \int_{-1}^{1} {}_{n}K_{ls}(r)\, \Omega(r, \cos\theta) \sin\theta P_{s}^{1}(\cos\theta)\, d(\cos\theta)\, r^{2} dr, \tag{3.26}$$

This defines the inverse problem as the LHS of this equation are the observed splitting coefficients the unknown rotation rate is on the RHS of the equation.

4. Regularized Least Squares Method

We now have an equation in terms of rotation rate and the splitting coefficients. We would like to solve this problem for the rotation rate so we write the rotation rate as an expansion in suitable basis functions. We will be using B-Splines in this project. Doing this will split up equation (3.26) into a system of linear equations in terms of the expansion coefficients of rotation rate. This can now be solved by a regularized least squares fit. Regularized least squares is a method that uses regularization to constraint solutions to a least square fit. To apply this method we first expand the rotation rate in terms of B-splines as mentioned before.

$$\Omega(r, \theta) = \sum_{ij} b_{ij} \phi_{i}(r)\, \psi_{j}(\cos\theta), \tag{4.1}$$

where ϕ_i and ψ_j are B-spline basis functions in r and $\cos\theta$. We can rewrite (3.26) into a system of equations involving the spline coefficients b_{ij} as follows:-

$$ {}_nc_{sl} = \sum_{i,j} b_{ij} \int_0^{\mathrm{R}_\odot} \phi_i(r) K_{ls}(r) r^2 dr \int_{-1}^{1} \psi_j(\cos\theta) \sin\theta P_s^1(\cos\theta) d(\cos\theta). \tag{4.2} $$

This gives a matrix equation of the form $Ab = c$ where b will contain the spline coefficients and c are the splitting coefficients. The elements of the matrix can be determined from (4.2). We also note that the angular integral can be calculated and stored in advance to save time when computing the matrix. We now have a system of linear equations. The rotation rate is a continuous function and therefore in principle has infinite degrees of freedom. This makes it impossible to solve with finite amount of data. This forces us to artificially introduce certain constraints to the rotation rate by controlling the smoothness of the functions. To this end we define a smoothing term as follows which is added to χ^2. By including them as rows in the matrix A they are automatically squared and minimized as part of the SVD routine. The smoothing terms are a measure of the smoothness of the function and are weighted by smoothing parameters.

$$ \chi^2 + \lambda_r \int_0^{\mathrm{R}_\odot} \left(\frac{d\Omega}{dr}\right)^2 Q_r(r) dr + \lambda_\theta \int_0^1 \left(\frac{d^2\Omega}{d(\cos\theta)^2}\right)^2 Q_\theta(\cos\theta) d(\cos\theta), \tag{4.3} $$

where λ_r and λ_θ are smoothing parameters which are to be manually fixed by trial and error and Q_r and Q_θ are weight functions to adjust where the smoothing is most effective. In our case the weight functions are simply $1/x$ of the respective variables, we use these two functions to heavily smooth the interior of the Sun where we have little data. The smoothing parameters λ_r and λ_θ are chosen by visually inspecting the rotation rate and by plotting the residual against a suitably chosen combination of l and ν. If the smoothing parameters are too large then the smoothness of the function will be maximized which can cause the loss of information. For appropriate finite smoothing the chosen derivative would tend to zero in regions where there is less information. We use a first order derivative in r and a second order derivative in $\cos\theta$. We use a first order derivative for the radial smoothing as we have nearly no data in the core ($< 0.2\mathrm{R}_\odot$). If we used a second order derivative and set it to zero then the rotation rate in the core will become a line with arbitrary constant slope whereas if we use a first order derivative then we get a constant rotation rate in the core which at least superficially lines up with the observation of solid body rotation in the interior of the Sun. We also add a condition

$$ \frac{d\Omega}{d\theta} = 0, \tag{4.4} $$

at the equator. This condition is added to ensure the symmetry in the rotation rate as we are only solving in one hemisphere.

5. Results

5.1 Rotation Rate

The smoothing parameters are determined by hand for this method. The fit is not particularly sensitive to the smoothing parameters near the correct values. Apart from simple inspection of the resultant rotation rate curves we can assess the performance of a pair of smoothing parameters from the residuals of the fit. Another method is to calculate and check the averaging kernels which will be discussed later. By plotting the residuals against suitable variables we obtain a plot which can inform us if the problem is over smoothed. We use the function $\log\left(\frac{\nu}{l+0.5}\right)$ which is a function of the lower turning point and plot it against residuals to obtain the following plot.

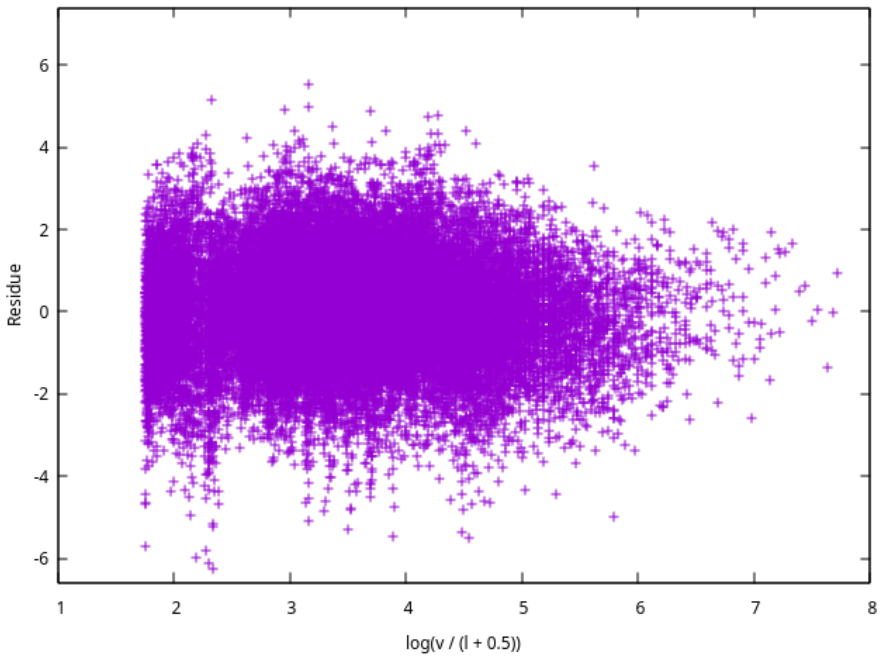

Figure 5.1: An example of log $\left(\frac{\nu}{l+0.5}\right)$ vs Residue plot when the smoothing is near its optimal values.

We have calculated the global rotation rate using 5 year data from HMI. This allows us to resolve many features such as the core rotation which would have been impossible to resolve in shorter data sets like the 3 month long sets used in temporal variance.

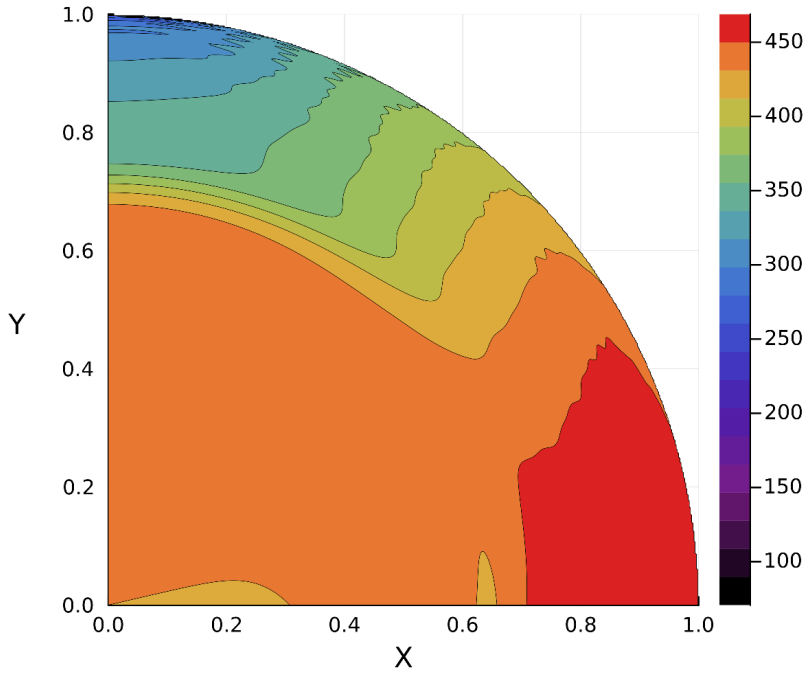

Figure 5.2: In this plot we see the rotation rate of a part of the Sun. Due to symmetry the rotation rate can be inferred in the other regions of the Sun using this plot. The x-axis is along the equator and the y-axis is parallel to the rotation rate. Both axes are in units of solar radius. We note that the differential rotation is easily seen and so is the solid body rotation of the interior of the Sun. We can roughly see the existence of the Tachocline but the exact position cannot be determined through inversion techniques.

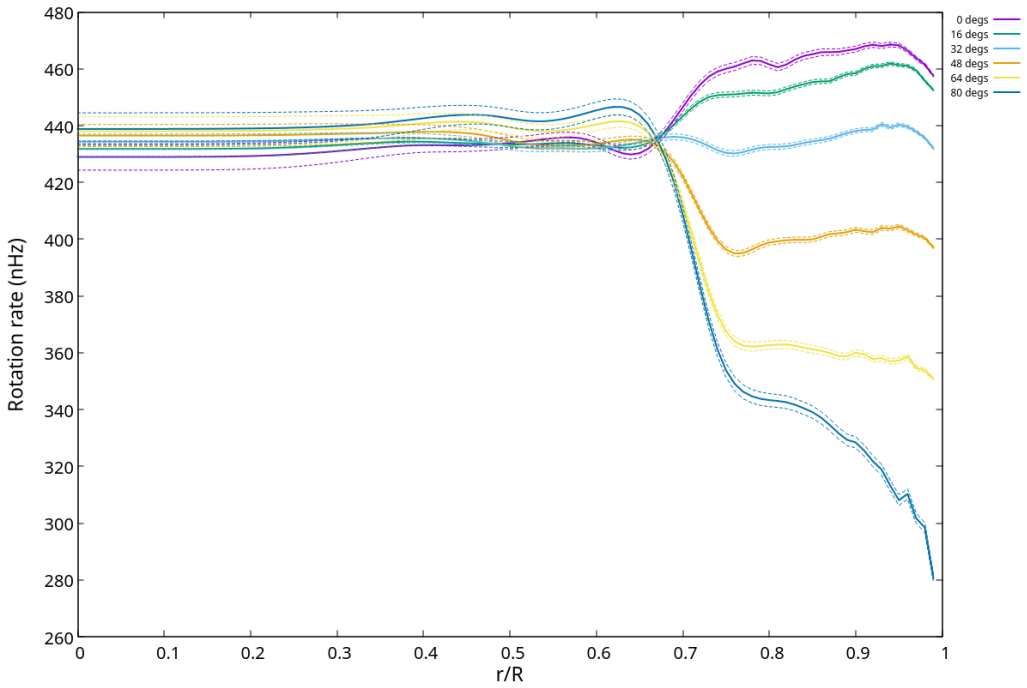

Figure 5.3: Here the same data from above can be better illustrated as cuts in r and theta. Here we have a plot which shows variation of rotation rate with radius at different latitudes. The 2σ error in the plot is depicted as dotted lines on both sides of each plot. We note that the error is larger in the interior. This is due to the fact that there is lesser information on the solar interior as most modes do not penetrate the core.

5.2 Averaging Kernels

The rotation rate at any r_0 and θ_0 can be written as a linear combination of the splitting coefficients. We can use the coefficients of this expansion to define a quantity called the Averaging Kernel which depends on r_0, θ_0, r and θ. They provide a useful tool for assessing the reliability of an inversion for a data set as if the smoothing is optimal then the averaging kernels will be sharply peaked around r_0 and θ_0. The averaging kernel also depends on the error in the data. In OLA (Optimally Localized Averages) inversion these averaging kernels are what are fitted.

If we assume that there are M splitting coefficients c_i from which we infer the rotation rate. This can be written in the following alternate form Howe [2009]:-

$$c_i = \int_0^{\mathrm{R}_\odot} \int_{-1}^{1} K_i\left(r, \cos\theta\right) \Omega\left(r, \cos\theta\right) dr\, d\left(\cos\theta\right) + \epsilon_i. \tag{5.1}$$

The solution of rotation rate a given r_0 and θ_0 is a linear combination of c_i which can be written as:-

$$\bar{\Omega}\left(r_0, \cos\theta_0\right) = \sum_{i=1}^{M} \alpha_i\left(r_0, \cos\theta_0\right) c_i = \boldsymbol{\alpha}^T \boldsymbol{c}, \tag{5.2}$$

where α_i are coefficients of expansion. Substituting (5.2) into (5.1) we get:-

$$\bar{\Omega}\left(r_0, \cos\theta_0\right) = \int_0^{\mathrm{R}_\odot} \int_{-1}^{1} \mathcal{K}\left(r_0, \cos\theta_0; r, \cos\theta\right) \Omega\left(r, \cos\theta\right) dr d\left(\cos\theta\right) + \epsilon_i, \tag{5.3}$$

where $\mathcal{K}\left(r_0, \theta_0; r, \cos\theta\right)$ is the averaging kernel given by

$$\mathcal{K}\left(r_0, \cos\theta_0; r, \cos\theta\right) = \sum_{i=1}^{M} \alpha_i\left(r_0, \cos\theta_0\right) K_i\left(r, \cos\theta\right). \tag{5.4}$$

Averaging kernels are independent of the values of data. They depend on the modes present in the data set and their errors as in χ^2 we divide each equation by its error.

To calculate them using quantities computed in RLS method we use equation (4.1) to write

$$\bar{\Omega}(r_0, \theta_0) = \sum_k b_k \beta_k = \boldsymbol{\beta}^T \boldsymbol{b}, \tag{5.5}$$

where i and j have been contracted into a single index k and $\beta_k = \phi_i \psi_j$. From equation (4.2) we know that b_k can be calculated from $A\boldsymbol{b} = \boldsymbol{c}$. Using the Moore-Penrose inverse of A, (given as A^+) we can write

$$\boldsymbol{b} = A^+ \boldsymbol{c}, \tag{5.6}$$

which when substituted into (5.5) to give

$$\bar{\Omega}(r_0, \theta_0) = \boldsymbol{\beta}^T A^+ \boldsymbol{c}. \tag{5.7}$$

Comparing this and (5.2) we get an expression for the expansion coefficients of the averaging kernel as follows

$$\boldsymbol{\alpha} = \boldsymbol{\beta}^T A^+. \tag{5.8}$$

This allows us to compute the averaging kernels using the pseudoinverse of the matrix we use in SVD. This is easily accomplished using the SVD decomposition that we obtain as part of the solution.

As mentioned earlier the width of the peak of averaging kernel gives a measure of how good the inversion method is. If the smoothing is too high then the peak will be broad. If the smoothing is low then the peak will be sharper, however, it might introduce oscillations due to which secondary peaks might appear. The location of the peak is also relevant as if we are performing inversion in a location with less information then the peak will not appear where we target it. This is most easily seen near the poles and near the core. In contrast to this the averaging kernel is sharply peaked near the target values near the surface and equator.

We locate the peak of the averaging kernels at various radii and latitudes and use that to calculate the FWHM of the peak in both r and θ. We also note the upper and lower limit of the FWHM as the peak may be asymmetric. We also note down the location of the target peak and where it actually appeared in the inversion. This gives a measure of how good the inversion is at that point. Table 5.1 gives a list of these values calculated for the RLS inversion performed in this project. We see that the best resolution given by low FWHM is achieved at the equator and near the surface. This is due to the fact that most of the information obtained from the acoustic modes is from these regions.

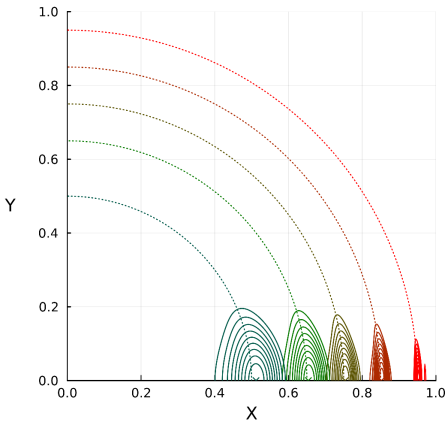

(a) $\theta = 0°$

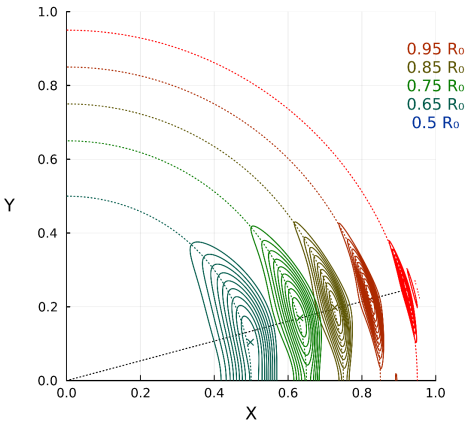

(b) $\theta = 15°$

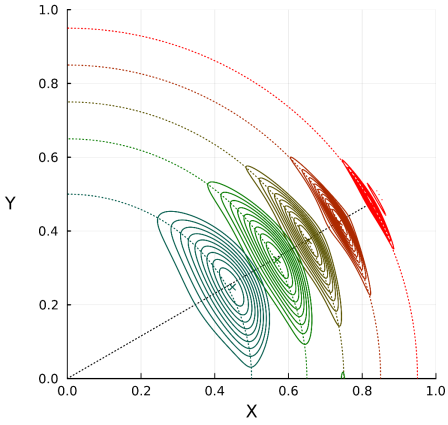

(c) $\theta = 30°$

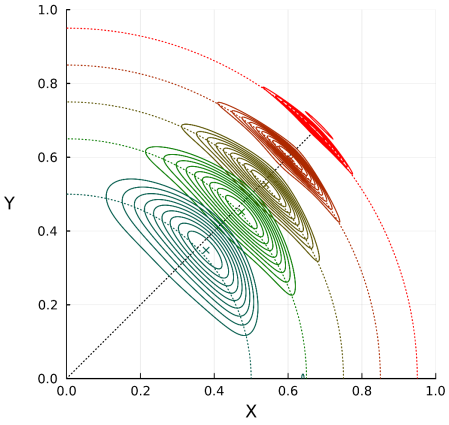

(d) $\theta = 45°$

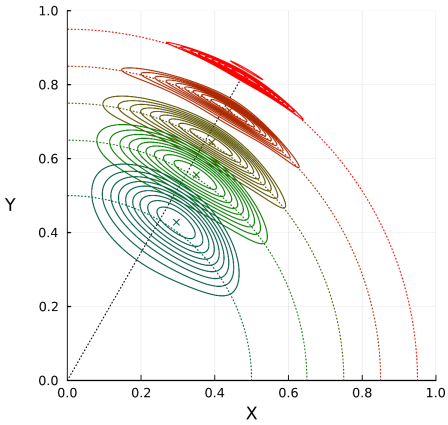

(e) $\theta = 60°$

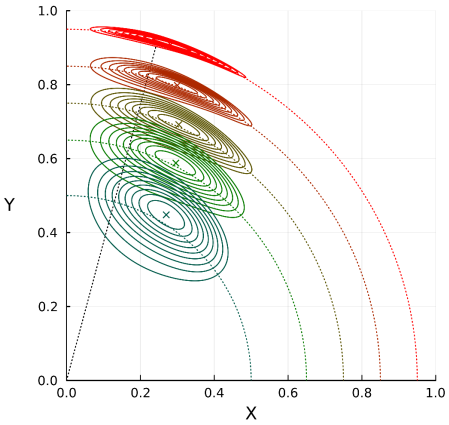

(f) $\theta = 75°$

Figure 5.4: Here we see the averaging kernels for the RLS inversion that was performed. The x-axis is along the equator and the y-axis is parallel to the rotation axis. The different colors show the averaging kernels at different depths and the different plots show the various latitudes. The dotted lines represent the radius and theta that the averaging kernels were supposed to peaked at. The cross mark shows where the averaging kernel actually peaked. The contours are drawn with levels from 10% to 100% of the maximum value to suppress the fluctuations at lower values. We note that the location of the peak of the averaging kernels deviate from the expected values when the latitude is near the poles. They also deviate near the core as there is less information there. The averaging kernels are most accurate near the equator and surface.

Table 5.1: Properties of averaging kernels - Position and resolution

Target Peak		Actual Peak		Peak max	r	Limits		θ	Limits	
r_0	θ_0	r	θ		FWHM	Upper	Lower	FWHM	Upper	Lower
0.95	0	0.950	0.0	846.2	0.012	0.956	0.944	8.206	4.103	-4.103
0.95	15	0.951	15.1	340.9	0.012	0.956	0.944	9.365	19.540	10.176
0.95	30	0.951	29.9	374.7	0.013	0.957	0.944	9.027	34.459	25.432
0.95	45	0.950	44.8	381.2	0.012	0.956	0.945	10.590	50.210	39.620
0.95	60	0.951	59.1	378.5	0.014	0.957	0.943	13.968	66.833	52.865
0.95	75	0.951	72.7	532.2	0.016	0.958	0.943	16.237	80.696	64.459
0.90	0	0.902	0.0	409.5	0.020	0.910	0.890	9.675	4.838	-4.838
0.90	15	0.901	15.1	162.0	0.021	0.911	0.890	11.580	20.645	9.065
0.90	30	0.901	29.8	173.5	0.022	0.911	0.889	11.195	35.597	24.402
0.90	45	0.901	44.7	176.5	0.022	0.911	0.890	12.978	51.400	38.421
0.90	60	0.901	59.2	174.6	0.025	0.913	0.888	16.704	68.104	51.400
0.90	75	0.902	71.2	260.6	0.029	0.915	0.886	18.001	80.183	62.182
0.85	0	0.852	0.0	246.0	0.030	0.866	0.836	11.609	5.804	-5.804
0.85	15	0.851	15.0	96.5	0.029	0.865	0.836	14.151	21.977	7.826
0.85	30	0.851	29.9	100.6	0.031	0.866	0.835	14.150	36.978	22.827
0.85	45	0.851	44.4	102.1	0.033	0.867	0.834	15.937	52.915	36.978
0.85	60	0.852	58.9	102.1	0.035	0.869	0.833	20.248	69.822	49.574
0.85	75	0.853	69.4	158.1	0.041	0.872	0.831	19.750	79.455	59.705
0.80	0	0.802	0.0	160.4	0.038	0.820	0.782	13.470	6.735	-6.735
0.80	15	0.801	15.0	62.4	0.038	0.820	0.782	16.547	23.424	6.877
0.80	30	0.802	29.8	63.9	0.040	0.821	0.781	16.949	38.326	21.376
0.80	45	0.802	44.3	65.1	0.041	0.822	0.781	18.975	54.330	35.355
0.80	60	0.803	58.6	67.5	0.046	0.825	0.778	23.396	71.430	48.034
0.80	75	0.804	67.8	105.4	0.053	0.828	0.775	21.363	78.662	57.299
0.75	0	0.754	0.0	111.2	0.048	0.776	0.728	15.351	7.676	-7.676
0.75	15	0.753	15.3	42.8	0.047	0.775	0.728	19.197	24.998	5.802
0.75	30	0.753	29.8	43.6	0.050	0.776	0.727	20.089	39.825	19.736
0.75	45	0.754	44.2	44.4	0.053	0.778	0.725	21.988	55.593	33.605
0.75	60	0.754	58.7	48.3	0.058	0.781	0.723	26.066	72.574	46.507
0.75	75	0.756	66.3	73.7	0.066	0.786	0.720	22.998	77.831	54.834
0.70	0	0.704	0.0	80.1	0.060	0.732	0.672	17.418	8.709	-8.709
0.70	15	0.704	15.5	30.4	0.058	0.730	0.673	22.491	26.565	4.074
0.70	30	0.704	29.6	31.1	0.061	0.732	0.672	23.184	41.309	18.125
0.70	45	0.704	43.8	31.5	0.065	0.735	0.669	24.921	56.806	31.885
0.70	60	0.706	58.2	36.1	0.072	0.739	0.667	28.052	73.052	45.000
0.70	75	0.708	64.7	53.2	0.081	0.744	0.663	24.592	77.102	52.511
0.65	0	0.654	0.0	61.3	0.072	0.688	0.616	19.445	9.723	-9.723
0.65	15	0.654	15.1	23.0	0.067	0.686	0.619	27.979	27.979	0.000
0.65	30	0.655	29.5	23.8	0.071	0.688	0.617	25.765	42.532	16.767
0.65	45	0.655	43.6	23.8	0.078	0.692	0.614	27.532	57.865	30.332
0.65	60	0.657	57.8	28.5	0.086	0.697	0.611	29.296	73.051	43.755
0.65	75	0.658	63.3	40.5	0.095	0.702	0.607	25.919	76.470	50.551
0.60	0	0.606	0.0	48.2	0.082	0.644	0.562	21.426	10.713	-10.713
0.60	15	0.605	15.1	18.0	0.076	0.641	0.565	29.461	29.461	0.000
0.60	30	0.605	29.3	18.8	0.082	0.644	0.562	28.187	43.793	15.606
0.60	45	0.607	43.3	18.5	0.088	0.648	0.560	30.512	59.199	28.686
0.60	60	0.609	57.2	22.9	0.100	0.655	0.555	30.740	72.925	42.184
0.60	75	0.611	62.1	31.5	0.108	0.661	0.553	27.367	75.828	48.460

Target Peak		Actual Peak		Peak max	r	Limits		θ	Limits	
r_0	θ_0	r	θ		FWHM	Upper	Lower	FWHM	Upper	Lower
0.50	0	0.512	0.0	28.8	0.105	0.561	0.456	26.429	13.215	-13.215
0.50	15	0.509	11.8	11.4	0.096	0.553	0.457	31.814	31.814	0.000
0.50	30	0.512	29.0	11.4	0.106	0.561	0.455	32.949	46.436	13.487
0.50	45	0.514	42.6	11.1	0.113	0.566	0.453	37.609	62.447	24.839
0.50	60	0.520	55.3	14.4	0.129	0.579	0.450	33.880	72.189	38.309
0.50	75	0.523	58.9	18.5	0.136	0.585	0.449	30.693	74.265	43.572
0.40	0	0.424	0.0	17.0	0.137	0.487	0.350	33.028	16.514	-16.514
0.40	15	0.418	0.0	8.3	0.127	0.475	0.348	30.355	30.355	0.000
0.40	30	0.425	29.9	6.4	0.136	0.487	0.351	41.645	52.197	10.552
0.40	45	0.429	42.9	7.5	0.151	0.499	0.348	42.132	65.113	22.981
0.40	60	0.439	51.7	9.6	0.166	0.515	0.349	38.655	70.602	31.947
0.40	75	0.443	54.4	11.4	0.171	0.522	0.351	36.070	72.137	36.067

Note: In this table all the radii are in units of $R_\odot$ and all angles are in units of degrees.

5.3 Temporal Variation

The analysis up to this point have been using the 5 year data obtained from HMI. While this allows us to resolve more details that we would not see in smaller duration data sets, we lose information on temporal variation of rotation rate. To study this variation 3 month long data sets from GONG spanning nearly 30 years have been used. This lets us see changes over at least two complete solar cycles. From this data we expect to see an overall butterfly-like pattern close to the surface to match the pattern seen in occurrence of sunspots. It is thought that this variation arises from interactions with the magnetic field inside the Sun. Covas et al. [2000] show that the toroidal component of magnetic field at $r = 0.95R_\odot$ of a mean field dynamo model gives the same butterfly diagram that is observed in rotation rate. In fact the poleward movement of rotation rate was also seen first in this dynamo model.

We calculate the rotation rate in the same way we did for the 5 year case but for 300 GONG months from 1995 to 2025. Since the duration of observation is lesser that the HMI data it will be difficult to resolve the core rotation. Once we have calculated the rotation rate for all 300 GONG months we then calculate the average rotation rate over each of the two complete solar cycles in the data set. The first complete solar cycle starts in August 1996 and the second starts in December 2008. This corresponds to the 11th and 140th GONG month in our data set. We compute two averages over these two cycles and subtract it to get the mean variation of the rotation rate as follows.

$$\Delta\Omega\left(r, \cos\theta\right) = \Omega\left(r, \cos\theta\right) - \left\langle\Omega\left(r, \cos\theta\right)\right\rangle. \tag{5.9}$$

The first average is used for the incomplete cycle before the 1996 and the second is used till 2025. This is then converted to rotational velocity using

$$v_\phi = 2\pi\left(\Delta\Omega\right) r\cos\theta. \tag{5.10}$$

This is then plotted in various ways as shown below.

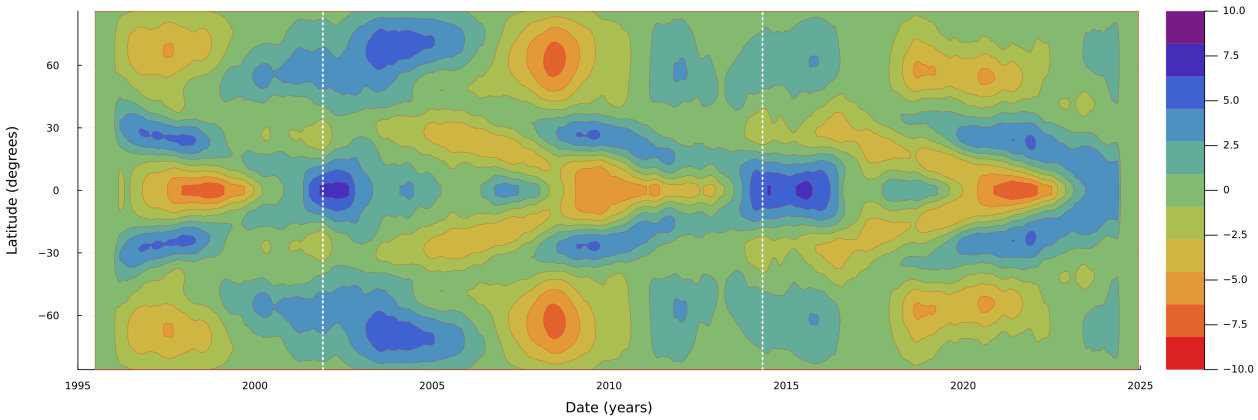

(a) $r = 0.98$

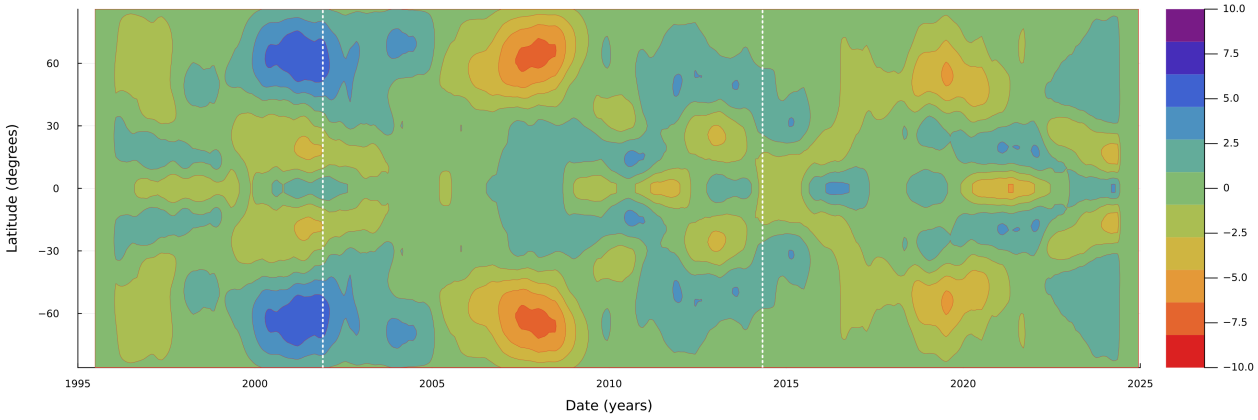

(b) $r = 0.9$

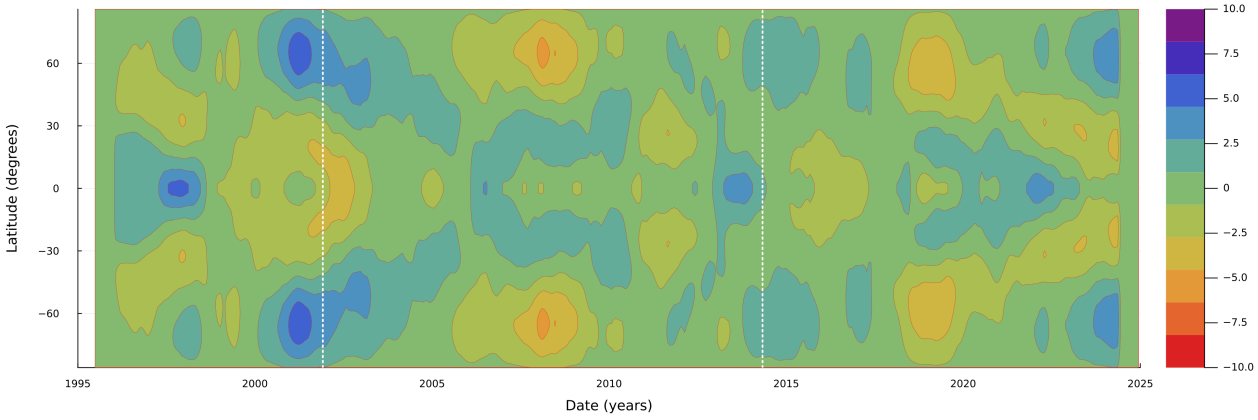

(c) $r = 0.8$

Figure 5.5: In this plot and the next the vertical dotted white line shows the start of both of the solar cycles when the solar activity was at its minimum. Here we see the latitude variation of the rotational velocity over time at fixed radii. We see that a butterfly like pattern is visible near the surface as seen in (a). We notice that this pattern does continue in deeper regions however the pattern is less clear. The pattern at $r = 0.98$ can be correlated with the appearance of sunspots.

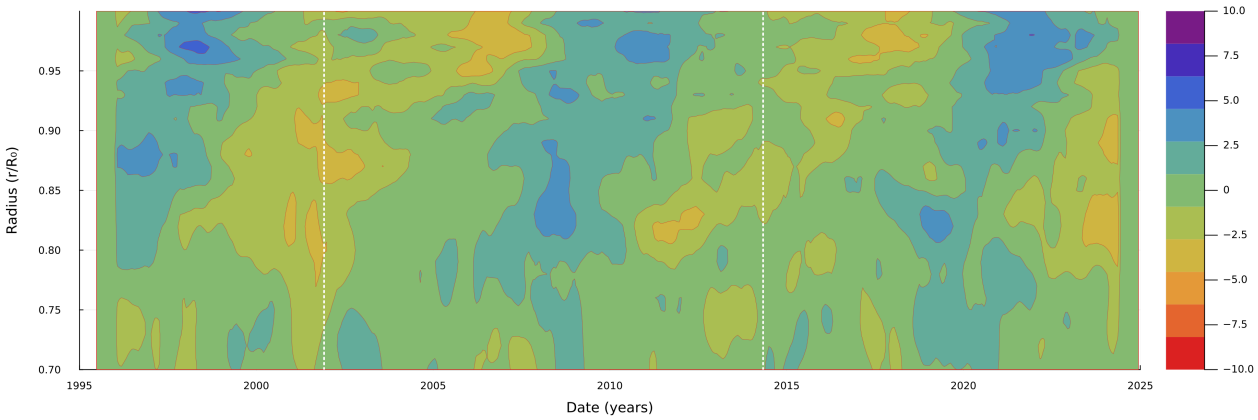

(a) $\theta = 20°$

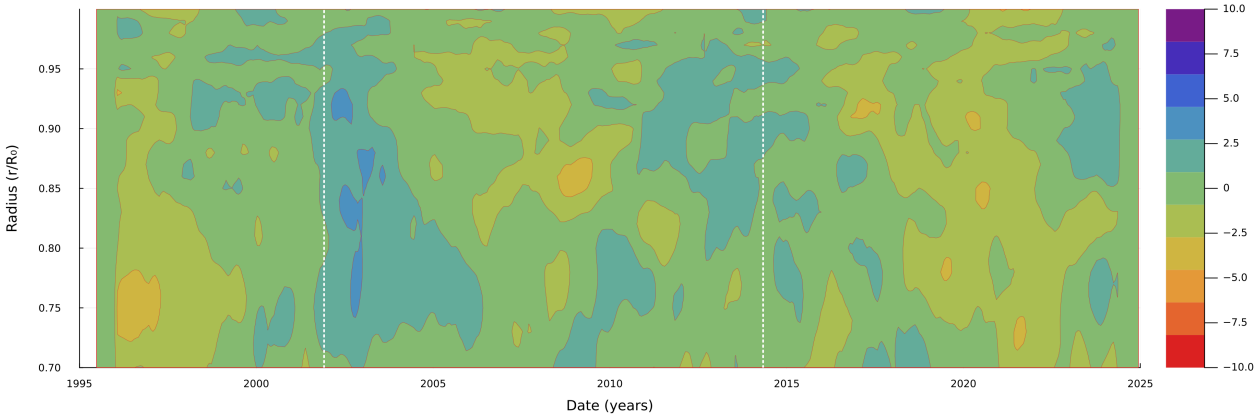

(b) $\theta = 40°$

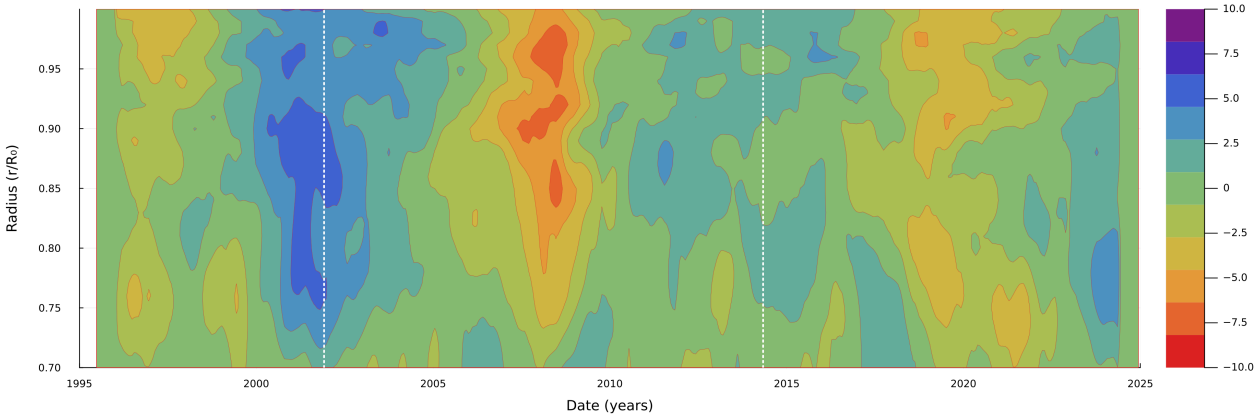

(c) $\theta = 60°$

Figure 5.6: Here we have plotted the variation of rotational velocity with radius over time. Here we have shown only the variation in the range $0.7R_\odot$ to $1R_\odot$ as due to the short duration of observations used the core rotation is not reliable. We see that at $\theta = 20°$ there is evidence of a slight upward movement.

Bibliography

S. Chandrasekhar. The Dynamical Instability of Gaseous Masses Approaching the Schwarzschild Limit in General Relativity. 140:417, August 1964. doi: 10.1086/147938.

E. Covas, R. Tavakol, D. Moss, and A. Tworkowski. Torsional oscillations in the solar convection zone. 360:L21–L24, August 2000. doi: 10.48550/arXiv.astro-ph/0010323.

F. L. Deubner. Observations of low wavenumber nonradial eigenmodes of the sun. 44(2):371–375, November 1975.

J. W. Harvey, F. Hill, R. P. Hubbard, J. R. Kennedy, J. W. Leibacher, J. A. Pintar, P. A. Gilman, R. W. Noyes, A. M. Title, J. Toomre, R. K. Ulrich, A. Bhatnagar, J. A. Kennewell, W. Marquette, J. Patrón, O. Saá, and E. Yasukawa. The global oscillation network group (gong) project. *Science*, 272(5266):1284–1286, 1996. doi: 10.1126/science.272.5266.1284. URL https://www.science.org/doi/abs/10.1126/science.272.5266.1284.

Rachel Howe. Solar Interior Rotation and its Variation. *Living Reviews in Solar Physics*, 6(1):1, December 2009. doi: 10.12942/lrsp-2009-1.

J. W. Leibacher and R. F. Stein. A New Description of the Solar Five-Minute Oscillation. 7:191–192, January 1971.

Robert B. Leighton, Robert W. Noyes, and George W. Simon. Velocity Fields in the Solar Atmosphere. I. Preliminary Report. 135:474, March 1962. doi: 10.1086/147285.

Michael H. Ritzwoller and Eugene M. Lavely. A Unified Approach to the Helioseismic Forward and Inverse Problems of Differential Rotation. 369:557, March 1991. doi: 10.1086/169785.

P. H. Scherrer, J. Schou, R. I. Bush, A. G. Kosovichev, R. S. Bogart, J. T. Hoeksema, Y. Liu, T. L. Duvall, J. Zhao, A. M. Title, C. J. Schrijver, T. D. Tarbell, and S. Tomczyk. The Helioseismic and Magnetic Imager (HMI) Investigation for the Solar Dynamics Observatory (SDO). 275(1-2):207–227, January 2012. doi: 10.1007/s11207-011-9834-2.

Roger K. Ulrich. The Five-Minute Oscillations on the Solar Surface. 162:993, December 1970. doi: 10.1086/150731.